Kovářík, Tomáš ; Bělský, Petr ; Rieger, David ; Ilavsky, Jan ; Jandová, Věra ; Maas, Michael ; Šutta, Pavol ; Pola, Michal ; Medlín, Rostislav

Particle size analysis and characterization of nanodiamond dispersions in water and dimethylformamide by various scattering and diffraction methods

Take down policy
If you believe that this document or any material on this site infringes copyright, please contact publizieren@suub.uni-bremen.de with full details and we will remove access to the material.

Particle size analysis and characterization of nanodiamond dispersions in water and dimethylformamide by various scattering and diffraction methods

Tomáš Kovářík ⓘ · **Petr Bělský · David Rieger ·**
Jan Ilavsky · Věra Jandová · Michael Maas ·
Pavol Šutta · Michal Pola · Rostislav Medlín

Abstract Over the past few decades, detonation nanodiamonds (NDs) have gained increased attention due to their unique physicochemical properties. Various methods for preparation of ND suspensions have been introduced. This paper presents thermally annealed nanodiamonds dispersed via sonication and separated by centrifugation in deionized water and dimethylformamide in five weight concentrations ranging from 0.05 to 1 wt%. Thermogravimetric analysis (TGA) and differential scanning calorimetry (DSC) were applied to study the thermal behavior of NDs. Crystallographic properties of air-annealed and dispersed NDs were examined by means of X-ray diffraction (XRD). Nanodiamond dispersions were analyzed by static light scattering (SLS), dynamic light scattering (DLS), ultra-small- and small-angle X-ray scattering (USAXS/SAXS), and high-resolution transmission electron microscopy (HRTEM). SLS and DLS give similar results of ND$^-$ aggregates mean size between ~ 61 and 73 nm, regardless of solvent type and nanoparticle concentration. For dispersions with increasing concentrations of NDs, neither increased aggregate size nor different kinetics of separation during sonication and centrifugation were observed. USAXS/SAXS provided the aggregates size ($2R_g$) in the range from 57 to 65 nm and size of primary particles from 5.4 to 5.8 nm. HRTEM also showed presence of larger aggregates with tens of nanometers in size in both water and DMF dispersions, and size of primary particles ranging from 5.5 to 6 nm in very good agreement with SAXS.

T. Kovářík (✉) · P. Bělský · D. Rieger · P. Šutta ·
M. Pola · R. Medlín
New Technologies – Research Centre, University of West
Bohemia, Univerzitní 8, 306 14 Pilsen, Czech Republic
e-mail: toko@ntc.zcu.cz

J. Ilavsky
Advanced Photon Source, Argonne National Laboratory,
Argonne, IL 60439, USA

V. Jandová
Institute of Chemical Process Fundamentals, ASCR, v.v.i,
16502 Prague, Czech Republic

M. Maas
Advanced Ceramics, University of Bremen, Am Biologischen
Garten 2, 28865 Bremen, Germany

M. Maas
MAPEX–Center for Materials and Processes, University of
Bremen, Am Fallturm 1, 28359 Bremen, Germany

Introduction

Nanodiamond (ND) is a member of a diverse family of nanocarbon allotropes that includes nanographite, nanotubes, fullerens, graphene, and other varied nanostructural modifications such as carbon onions and semi-crystalline/amorphous carbon (Ioni et al. 2011; Aqel et al. 2012; Zeiger et al. 2016; Phiri et al. 2017). ND particles attracted extensive research interest because of valuable properties such as superior mechanical strength (Shakun et al. 2014), crystallinity, chemical stability (Mochalin et al. 2012), electric resistivity (Kondo et al. 2013), and antibacterial (Maas 2016) and luminescent properties (Kaur and Badea 2013). Besides, ND particles possess a highly reactive surface surrounding their diamond core, containing a wide variety of chemical functional groups. In the case of detonation ND, the surface of nanoparticles may contain oxygen-containing groups such as carboxylic acids, esters, ethers, lactones, and amines. In addition, the surface of nanodiamonds (NDs) is partially covered by thin layers of graphitic or graphene-like structures (Krueger 2008).

It was shown that the surface of NDs can be homogenized using oxidative (oxidizing acids, thermal oxidation) or reductive (hydrogenation, hydrogen plasma treatment, borane reduction) methods and concurrently selective functional groups can be installed on the surface of primary particles and/or on the outer side of larger agglomerates (Shenderova et al. 2002; Krueger et al. 2005). Many authors have reported a variety of other chemical reactions for functionalizing ND surfaces, mostly with an intent of covalent/non-covalent immobilization and subsequent grafting of complex moieties or larger biomolecules (Liu et al. 2004). For example, fluorination can be performed in a gas phase reaction of F_2/H_2 mixtures at elevated temperatures or atmospheric pressure plasma (Ray et al. 2007) and chlorination by photochemical reaction of gaseous chlorine with hydrogenated surface (Sotowa et al. 2004). Moreover, a silanization technique using (3-aminopropyl)trimethoxysilane (APS) was applied to obtain the covalent attachment of amino acids to the diamond surface. This modification allows efficient grafting of larger bioactive macrostructures such as enzymes or proteins (Krueger et al. 2006).

The versatility of the approaches is also linked to the dispersibility of NDs in different solvents, their particle size distribution, and type of applications. Water represents the most common dispersing medium for investigation of different techniques for deagglomeration and characterization of nanodiamond dispersion. A method for effective de-aggregation was reported consisting in stirred media milling and subsequent sonication, where the average value of particle size distribution of diluted aqueous suspension (0.2%) reached 5.3 nm, after sonication for 1 h (Krueger et al. 2005). Further, bead assisted sonic disintegration (BASD) was found to be an efficient technique to achieve primary particles of NDs in diverse protic/aprotic solvents, including water. Dispersibility of the ND particles in highly polar alcohols and polar or hydrocarbon solvents exemplified the viability of these nanosuspensions with particle size ranging from 4 to 100 nm (Ozawa et al. 2007). The less time-consuming BASD procedure using silica beads and short pulses of high-power sonication was applied to disaggregate agglomerates from ~ 1 μm to < 100 nm (Pedroso-Santana et al. 2017). It was reported that the ball-milling technique has been performed with different milling media: ammonium bicarbonate, sodium chloride, and sucrose, followed by dispersion in ethanol, water, and dimethyl sulfoxide (Khan et al. 2016). Also, bead-milling of oxidized ND with the addition of surfactants was examined using oleylamine (OLA), octadecylamine (ODA), and oleic acid (OA). It resulted in similar dispersions, where particle size distribution of OLA suspensions and ODA suspensions showed a median size of 22.8 and 45.1 nm, respectively (Li and Huang 2010).

However, mechanical deagglomeration methods suffer from difficulties such as contamination of ND colloids with abrasion debris from milling beads (zirconia, alumina, silica) or ultrasonic treatment (titanium), loss of carbonaceous material during impurity removal, or bi/trimodal particle size distribution. Due to the above-mentioned difficulties of the mechanical methods, chemical deagglomeration of thermally annealed NDs using the arylation technique was investigated. Arylation with functionalized aryl diazonium salts carrying COOH, SO_3H, NO_2 groups led to synthesis of water and/or acetone-based ND colloids with particle sizes in the range of 25–50 nm (Liang et al. 2011). Other authors publish results where purification and annealing were performed in hydrogen. By annealing aggregated NDs in hydrogen gas, the aggregates > 100 nm are broken. After centrifugation above 10,000 rpm, the particle size distribution shifted to 2–4 nm (Oliver et al. 2010).

2

Recently, an extreme reduction of size of NDs below 2 nm was presented. This procedure consists of oxidative annealing at 520 °C for 25 min followed by sonication-centrifugation treatment at 120 W and 13,124×g, respectively (Stehlik et al. 2016). Likewise, a method for the synthesis of an ultrafine fraction of NDs in deionized water using ultracentrifugation was introduced. A protocol of 3 h ultracentrifugation with the maximum gravitational field at the bottom of the tube reaching 215,000×g resulted in a fraction of NDs with a narrow size distribution ranging from 6 to 9 nm (Koniakhin et al. 2017).

To obtain reliable data concerning structural state, surface area properties, and particle size distribution of NDs in diverse solvents, the materials were characterized by multiple techniques such as XRD for lattice/phase parameters determination, XPS for dopants and surface functional groups description (Shenderova et al. 2011), PSD and BET for analysis of nanoparticles distribution, arrangement, and interactions (Singh et al. 2016), SAXS for identification of structural parameters including shape and size of nanoparticles (Ten et al. 2012), HRTEM for imaging of particles and structural pattern orientation (Turner et al. 2009), DLS for investigation of particle size distribution (Pichot et al. 2013), and many more. In addition, other studies are aimed at determining the elemental composition on nanodiamonds and screening for elemental impurities of commercial NDs by emission spectroscopy and ICP-MS, respectively (Mitev et al. 2014; Volkov et al. 2014).

It has been reported that conventional nanodiamond powder shows a complex multilevel fractal-like structure exhibiting self-similarity under variation of scale (Vul and Shenderova 2014). Besides higher-level agglomerates (> 10 μm), the fractal structure is assembled of different-level aggregates that are classified as a secondary size (2–3 μm) and/or primary size (100–200 nm) including primary particles (4–5 nm) (Osawa 2008). Furthermore, it has been stated that lower-level aggregates have the form of agglutinates (covalently bonded aggregates), so-called strongly bound aggregates, up to a size of 300 nm (Osawa 2008; Paci et al. 2013).

Here we report a study of thermally annealed nanodiamonds dispersed via sonication and separated through centrifugation in polar solvents (dispersing media), i.e., deionized water and dimethylformamide in five weight concentrations ranging from 0.05 to 1 wt%. The primary goal of the presented work was to examine the influence of the dispersing medium and ND concentration on the aggregation behavior of NDs (size and internal structure of ND aggregates) by mean of scattering techniques. Also, the aim of this work is to describe in detail the influence of various concentrations on aggregate size and formation in two different solvents. SLS, DLS, and SAXS/USAXS were used for this purpose. Also, the size and structural parameters of primary ND particles were examined using several different methods. SEM and HRTEM/SAED analyses were performed to obtain visual and structural characterization of both the aggregates and the primary particles. XRD was applied to investigate the phase composition. Thermal analysis (TGA, DSC) was applied for a thorough study of the kinetics of the thermal behavior of NDs. The results of the used methods are compared with each other and the observed differences are discussed.

Experimental

Materials and preparation of dispersions

Powder of grade G01 detonation NDs was purchased from PlasmaChem GmbH (Lot# YF14101). Bulk density of 0.69 g/cm^3, pycnometric density of 3.18 g/cm^3, and specific surface (BET) of min. 350 m^2/g are guaranteed by material safety data sheet. In-house prepared deionized water (DI) with resistivity of 14.3 MΩ.cm (Demiwa 3, Watek, CZ) at 25 °C and N,N-dimethylformamide (DMF) from Sigma-Aldrich (anhydrous, 99.8%) were used as dispersing medium.

A scheme of the preparation of the nanodiamond dispersions is shown in Fig. 1. The surface of purchased NDs was modified via thermal treatment in air atmosphere to generate a negative surface charge through selective surface oxidation supplemented with remove the amorphous carbon and other non-diamond species. Negatively charged NDs (ND$^-$) were obtained by annealing at 450 °C for 3 h. Then, the annealed NDs$^-$ were dispersed in water and DMF, respectively. A Bandelin Sonopuls-Ultrasonic homogenizer HD 3200 was used to obtain the required dispersion of ND$^-$. An ultrasonic probe made of titanium alloy (Ti-Al6-V4) was used with an operating frequency of 20 kHz and an energy conversion of 400 kJ into each sample. Sonication for 3 h with continuous stirring was applied to obtain gray-colored nanodispersions. Afterwards, the solutions were centrifuged three times at 4000 rpm (2500×g) for 1 h and the pellets were discarded. The resulting dispersions
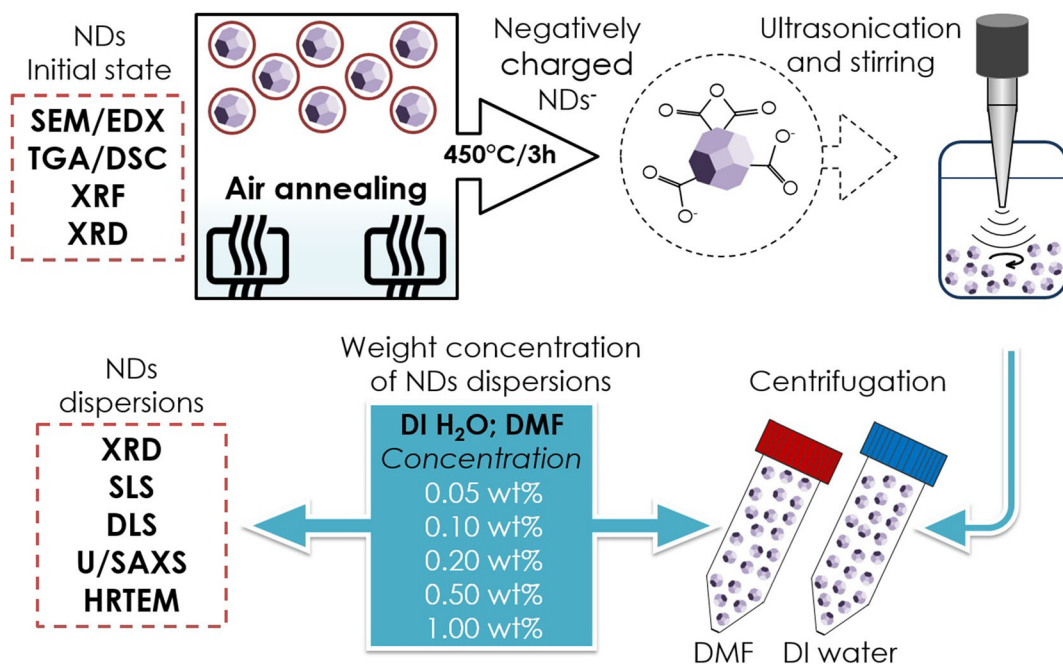
Fig. 1 Schematic synthesis route of nanodiamond dispersions and applied analytical tools

were prepared in five different concentrations ranging from 0.05 to 1 wt% for each solvent.

Methods

As shown in Fig. 1, the NDs were characterized at their initial state by scanning electron microscopy (SEM), energy dispersive X-ray spectroscopy (EDX), thermogravimetric analysis (TGA) and differential scanning calorimetry (DSC), and X-ray diffraction (XRD). The negatively charged ND^- after annealing in air and ND^- from the prepared dispersions (dried) were investigated with XRD. Dispersions were subjected to particle size analysis using static light scattering (SLS), dynamic light scattering (DLS), and small-angle X-ray scattering (SAXS) in combination with ultra-small-angle X-ray scattering (USAXS). A summary of all techniques in relation to what stage of processing and treatment the sample was prepared is given in Table S1 (Online Resource).

Thermal analysis

The effect of air annealing on NDs in initial state was investigated with TGA and DSC. TGA was performed using a TGA Q500 thermogravimetric analyzer (TA instruments), with a heating rate of 10 °C/min up to

800 °C, under air purge flow of 80 mL/min. DSC was carried out on a DSC Q200 differential scanning calorimeter (TA Instruments) under air flow of 80 mL/min and heating rate of 10 °C/min.

Elemental analysis and crystalline phase identification

Elemental composition of ND powder in initial state was investigated with wavelength dispersive X-ray fluorescence using a high-power benchtop sequential Rigaku Supermini200 spectrometer. XRF analysis was carried out under vacuum on pressed powder samples (1.5 t of pressure). Qualitative analysis for the detection of impurities was performed under long-term data collection conditions (1 h/sample). XRD analysis of untreated NDs, air-annealed, and ND^- dispersed in DI H_2O and DMF (dried) was performed using a PANalytical X'Pert Pro automatic powder diffractometer. This device uses a copper X-ray tube with Cu Kα radiation and an ultra-fast semiconductor detector PIXcel with high resolution and symmetrical Bragg–Brentano (θ–2θ) geometry. The 2θ measured range was set from 10° to 100°. The powder samples were measured in cuvettes ensuring an X-ray irradiation area of 10×10 mm. Central positions of diffraction lines were determined according to positions of peak maxima

and crystallite sizes according to Scherrer equation with constant K of 0.94.

Light scattering techniques

SLS was conducted on a Horiba LA-960 particle size analyzer to determine the particle size distribution. Measurements were performed in 15 mL fraction cell made of tempax glass at a wavelength of 405 nm for detection of particles below 100 nm. The optical depth of samples with concentration above 0.25 wt% was too high for the correct measurement and thus it was reduced by diluting these samples to the concentration of 0.25 wt%. The samples were measured immediately after the dilution process to avoid possible coagulation. Measurements of the nanodiamond particle size distribution by DLS were performed with Anton Paar Litesizer 500 instrument using polystyrene cuvettes for H_2O samples and quartz cuvette for DMF samples at wavelength of 658 nm. In order to minimize multiple scattering in DLS experiments, the optical depth of the samples was reduced by using the backscattering geometry with a scattering angle of 175°. Although the samples with lower ND concentrations (below 0.5 wt%) could have been measured in forward scattering geometry as well, all samples were measured in backscattering geometry to keep the same experimental setup. Results of DLS and SLS were expressed in volume distributions to avoid the possibility of error magnification introduced by conversion of intensity distributions to number distributions.

X-ray scattering techniques

SAXS experiments were conducted on a laboratory SAXSess mc^2 instrument (Anton Paar) equipped with a microfocus X-ray source with a Cu anode. The dispersion samples were filled and sealed in thin-walled borosilicate glass capillary tubes for X-ray diffraction. The exposure time was 30 min and the range of scattering vector magnitude q was 0.18–7 nm^{-1}. Size of primary ND particles was evaluated according to position of shoulder at q 0.1/A. Profiles of pure solvents were subtracted as background. USAXS experiments were carried out using USAXS/SAXS/WAXS instrument (Ilavsky et al. 2018) located at 9ID beamline at the Advanced Photon Source, Argonne National Laboratory, IL, USA. X-ray energy of 21 keV was used, data collection time was about 2 min, profiles of pure solvents were subtracted as background, and instrumental slit smearing was removed during data reduction. Intensity data were placed on absolute intensity scale.

Microscopy techniques

The samples were also studied by scanning electron microscopy using a Tescan VEGA3 SB instrument equipped with an energy dispersive X-ray (EDX) detector (integrated 4 silicon drift detector—SDD) and a JEOL JSM-7600F instrument with field emission (FESEM). The samples for FESEM were prepared by spraying of diluted dispersions on flat silicon wafer as substrate. The high-resolution transmission electron microscopy was conducted on a JEOL JEM-2200FS instrument applying an accelerating voltage of 200 kV. Samples were dispersed and collected on a Cu grid coated with amorphous carbon (mesh 300). The results of small area electron diffraction (SAED) were evaluated according to calibrated pixel size. Lattice parameters from HRTEM images were extracted by direct measurement and by fast furrier transform (FFT) of original images in ImageJ software.

Results and discussion

SEM/EDX

SEM images of NDs in initial state revealed the formation of dense and uniform powder with clump-like morphology. The diameter of the largest agglomerates was approximately between 5 and 50 μm. Bundles of smaller particles (< 1 μm) on the surface of larger clusters were also observed as seen in Fig. 2a, b EDX elemental mapping showed that in addition to the dominant carbon, uniform distribution of aluminum, silver, and chlorine are also present, as seen in Fig. 3a. EDX ZAF standardless quantification was performed over eight areas taken on random aggregates. The highest content of impurities was detected as follows: Al = 0.45–1.33 at% with minor amount of Ag = 0.12– 0.35 at%, Cl = 0.08–0.23 at%, Si = 0.01–0.08 at%, and S = 0.01–0.04 at%. Beyond this, notable content of $N <$ 2 at% and O < 7 at% was also detected, as presented in Fig. 3b. The occurrence of impurities can be mainly attributed to severe conditions associated with the detonation synthesis and subsequent oxidative isolation of nanodiamonds from the reaction soot (Mitev et al.
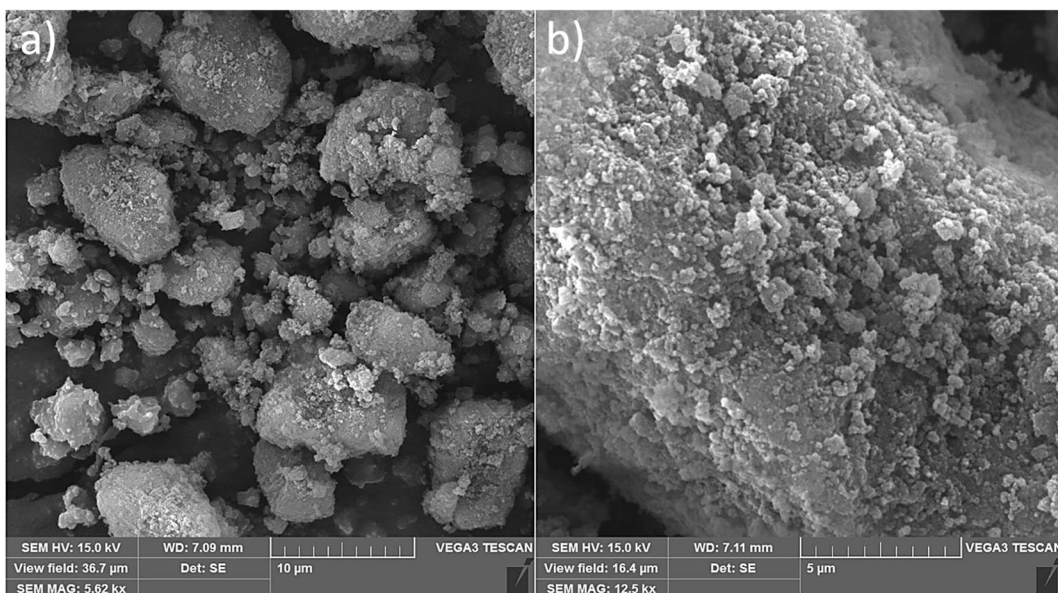
Fig. 2 SEM images of initial ND powder. **a** Larger agglomerates with **b** smaller bundles on the surface of clump-like clusters

2014). Also, the amount of impurities and their composition in NDs depend on the number of treatment stages and on the applied chemicals (Dolmatov et al. 2016).

It has been reported that different batches from different manufacturers have shown different contents of elements in ND samples (Volkov et al. 2014). Besides, the results of the chemical composition may differ due to the application of different analytical methods and quality and/or form of measured samples. With regard to these facts,

WDXRF was performed on pressed pellets of NDs in initial state. Total content of impurities was qualified at < 0.4 wt%. Measurement of impurities using the long-term qualification mode revealed the following elements, expressed in atomic percentage: Al 21.3%, Si 2.2%, S 5.1%, Cl 39.3%, and Ag 32.1%. This result confirms the presence of specific elements (Cl, Ag) and is consistent with HRTEM observations (see section "HRTEM/FESEM").
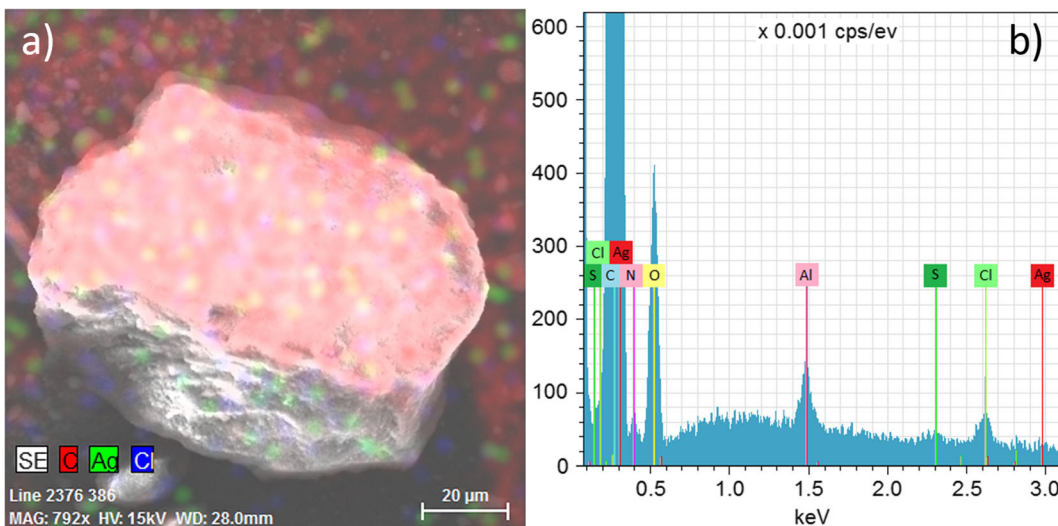

Fig. 3 SEM image/elemental mapping of nanodiamond agglomerate. **a** Initial state with clump-like morphology. **b** EDX spectrum of the elemental composition

Thermal analysis

Figure 4 shows TGA curve (green curve) indicating the first slight weight loss at temperatures below 100 °C which is attributed to the evaporation of adsorbed water (Liang et al. 2011). The kinetics of thermal behavior of NDs in initial state was also studied by DSC both in an open pan under an air flow of 80 mL/min and in a hermetically sealed pan. The measurement in the open pan (red-circle curve) showed an endothermic process in the range of 52–157 °C with a corresponding enthalpy of 63.55 J/g. Measurement of another sample in a hermetically sealed pan (blue-square curve) showed the same trend and the endothermic process merely shifted to higher temperatures in the range of 77–178 °C consuming a heat of 57.68 J/g. This shift is attributed to the delay of desorption processes in the sealed pan.

TGA and DSC curves indicate that with increasing temperature the desorption process continues up to ~ 300 °C, corresponding to a weight loss of 7.5% (Stehlik et al. 2015). The oxidation processes took place above 300 °C, which is well documented by the distinct onset of exothermic reactions, apparent from the DSC curve. The total heat flow at 450 °C amounted to 1.52 W/g. From the presented data can be concluded that above 300 °C, the rate of weight loss is partially reduced by

conversion of sp^2 carbons into various oxygen-containing groups with a subsequent combustion effect beginning above 450 °C (Huang et al. 2008).

The TGA curve indicates acceleration of degradation mechanism at temperatures above 455 °C, where the linear dependence of weight loss ends. The onset of major decomposition can be observed at 500 °C. Above that temperature, an intensive weight loss occurred due to oxidative etching where carbon is oxidized by oxygen in air to carbon dioxide (Stehlik et al. 2015). The DSC curve shows an increase of heat expressed as exothermic reaction up to 3.03 W/g at 500 °C. As expected, the sample with restricted access to air (hermetically sealed pan) showed a significantly lesser exothermic reaction with almost six-times lower heat flow 0.55 W/g at 500 °C, as presented in Fig. 4 (blue-square curve). TGA results showed a significant weight decrease in temperature zone 500–600 °C and documented incombustible residues ~ 0.8 wt% at 700 °C with insignificant changes up to 1000 °C.

Based on the thermal analysis results, it can be concluded that the applied heat treatment of the ND powder at 450 °C induced a significant surface oxidation. Thermal analysis results demonstrate that the temperature of applied air annealing lies just ahead of the threshold of major oxidative decomposition. Thus, the selective oxidation of the nanodiamond powder, including possible amorphous and graphite phases, was achieved as
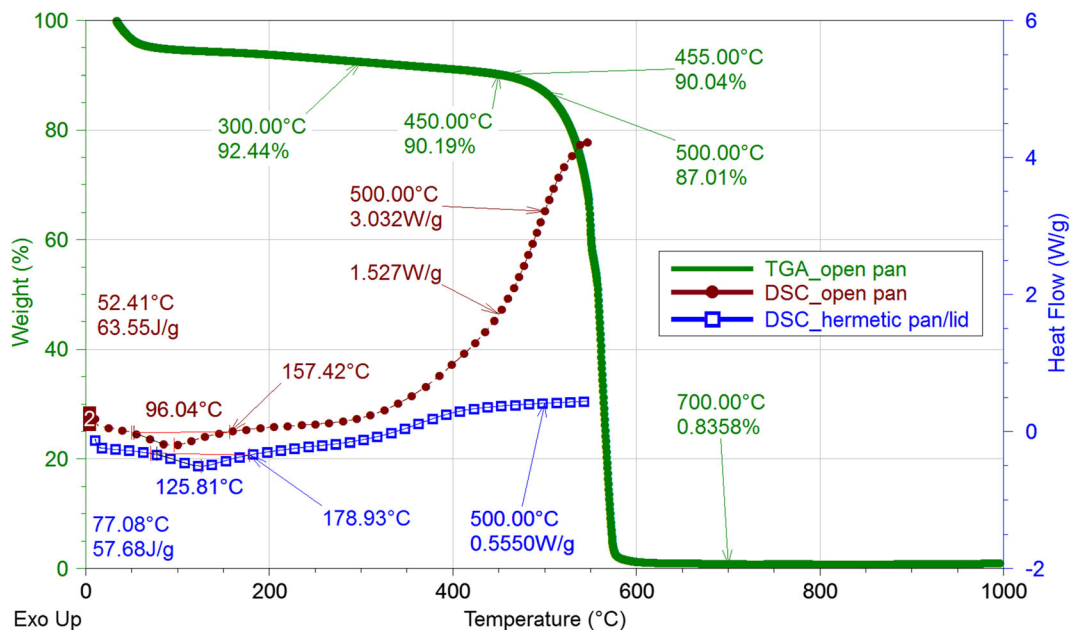

Fig. 4 Thermal behavior of NDs described by meaning of TGA and DSC

published elsewhere (Osswald et al. 2006). Oxidation for 3 h appears to be sufficient to remove the amorphous carbon and other non-diamond species (Osswald et al. 2008).

XRD

Figure 5 presents the XRD patterns of ND powder in initial state, after thermal treatment at 450 °C for 3 h in air atmosphere (ND⁻) and dispersed in DI H$_2$O and DMF—sonicated, centrifuged, and dried, respectively. XRD patterns show the typical intense diffraction lines of diamond with peak positions at 43.6° (111), 75.7 °C (220), and 91.2 °C (311) (Khan et al. 2016; Koniakhin et al. 2017).

Some impurities in the untreated NDs (initial state) were found in a small amount. Particularly, several diffraction lines showed the presence of silver chloride in the form of chlorargyrite. Also, a trace amount of alumina compounds was detected. These findings correspond to the results of the EDX mapping where the presence of aluminum, silver, and chlorine was also confirmed.

The particular micro-impurity investigation of NDs was presented elsewhere (Mitev et al. 2014). A notable content of Al and minor content of Ag were also detected at approximately 10 to 1 ratio determined by ICP-MS (Volkov et al. 2014). It should be noted that there were also noticeable variations in the content of Fe, Al, and Ag between different samples of the same manufacturer (Mitev et al. 2014).

The detected aluminum in NDs can be identified as transition forms of alumina namely the modifications gamma, delta, eta, and theta (γ, δ, η, θ-Al$_2$O$_3$), and boehmite which is aluminum oxide hydroxide in the form of γ-AlO(OH). Because of low volume fraction of material (below 1%) and similar diffraction patterns, it is not possible to exactly resolve which phases are present. However, it is very likely that the transition alumina is in the gamma modification because it is the first structural arrangement in the dehydroxylation process of boehmite (Lamouri 2017). Details of the lattice parameters of the individual phases in the initial state are given in Table S2 (Online Resource).

It is evident that thermal treatment at 450 °C does not lead to significant changes in the phase composition as presented in Fig. 5 (blue curve of ND⁻). This is due to the thermal stability of the individual crystalline phases such as alumina, chlorargyrite, metallic silver, and diamond. In the case of nanodiamonds, intense temperature decomposition has been shown to start above 500 °C, as confirmed by TGA. The exception is aluminum oxide hydroxide, which was not found in annealed state. It was because of its thermal decomposition (dehydroxylation) occurring in the temperature range from 300 to 480 °C (Kloprogge et al. 2002).

After sonication, centrifugation, and drying of water dispersion of ND⁻, only negligible traces of chlorargyrite could be detected as seen in the corresponding XRD pattern (dark blue curve), Fig. 5. These phenomena can be explained by the mechanism of dissolution and recrystallization of chlorargyrite in an aqueous medium. The solubility of AgCl in H$_2$O is

Fig. 5 XRD patterns of nanodiamond powder in initial state (ND⁰), air-annealed (ND⁻), and ND⁻ dispersed in H$_2$O and DMF (dried)
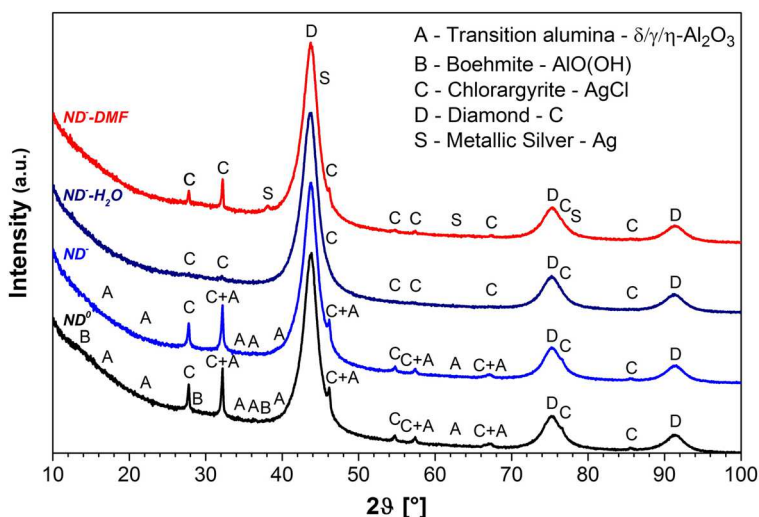
exceptionally low with a solubility constant of pK_{sp} of 9.75 at normal temperature. It can be anticipated that by increasing the temperature during the sonication, more than 20 wt% AgCl can be dissolved. Further, the solubility of AgCl increases with water pressure and AgCl is efficiently transported by water vapor (Migdisov et al. 1999; Akinfiev and Zotov 2016). Outside the ultrasonic field and during cooling of the suspension, AgCl can recrystallize and grow up to 100 nm (Ma 2014).

The XRD results of the dried DMF dispersions are slightly different. According to XRD patterns, the sonication and centrifugation process was not sufficient for the DMF dispersion to completely remove non-diamond impurities. However, compared to ND$^-$, there is a noticeable reduction in the content of alumina and chlorargyrite. Because of low solubility of chlorargyrite in DMF (pK_{sp} of 14.8), the presence of metallic silver in contrast to DI H$_2$O dispersions can be explained by surface reduction mechanism where the silver crystallites are formed on the surface of pristine chlorargyrite crystals (Chantooni and Kolthoff 1973; Song et al. 2013).

Both types of dispersions are characterized by a high proportion of diamond with typical intense diffraction lines (Xu et al. 2005). Moreover, diffraction profile of heat-treated NDs was analyzed, and based on the peak broadening, average crystallite sizes of nanodiamonds and chlorargyrite were determined as 4.1 and 61.4 nm, respectively.

Light scattering

Before the sonication process, the particle size distribution of heat-treated nanodiamond powder was determined by SLS. Figure 6 shows the particle size distribution after 10 min of magnetic stirring in water. The original nanodiamond powder consists of an approximately trimodal size distribution of aggregates in micrometer range—it can be well decomposed into three log-normal distributions with the individual median (D50) values of 1.7 μm (a fraction of finer particles), 15.6 μm, and 51.8 μm, which closely corresponds to the previous observations by SEM.

Aqueous and DMF dispersions of ND$^-$ were prepared in several weight concentrations ranging from 0.05 to 1 wt%, as described in Experimental section ("Materials and preparation of dispersions"). The resulting nanodispersions varied in color with slight differences between DI water and DMF. The diversity

in color was observed from the transparent appearance to dark brown/black, in relation to the increasing weight concentrations of the dispersions, as seen in Fig. 7. The transparency of the nanodispersions sharply decreases with increasing concentration which limits the methods using light scattering. In both cases, the theory in models applied for evaluation of SLS and DLS assumes only single scattering. However, the increasing optical density (OD) of the sample increases the probability of multiple scattering (Stevenson et al. 2016). Therefore, backscattering geometry was used for DLS and the samples for SLS concentrations above 0.25 wt% were diluted, as described in detail in the "Experimental" section ("Light scattering techniques"). The correctness of the technique of diluting the samples for SLS was verified by subsequent DLS measurement of diluted samples. DLS showed that the ND$^-$ aggregate size distribution before and after dilution did not differ.

Measurements of particle size distribution by SLS and DLS were performed on both series of ND$^-$ dispersions. Figure 8 shows representative particle size distributions of ND$^-$ dispersions with concentrations of 0.5 wt% in DI water and DMF. As seen, the DLS method provides slightly broader distribution curves compared to SLS. However, both methods give similar results of mean size between ~ 61 and 73 nm, regardless of solvent type and nanodiamond concentration.

The methods indicate only minor deviation in volume-weighted mean values across the measured concentrations and the used dispersing mediums. Thus, it can be concluded that the initial concentration does not affect the degree of aggregation of the resulting nanodispersions at the considered low particle concentration. Graphs in Fig. 9 show a comparison of the mean diameter for all concentrations in both solvents resulting from SLS and DLS, respectively. A small difference of the mean values can be observed for DMF, where a slightly smaller size of aggregates results.

Further, the D-Values (D10, D50, and D90) were evaluated from the obtained volume size distributions, which is the common metrics to describe particle size distributions. D50 is the median of the distribution, i.e., the particle diameter that 50% of the sample's volume is comprised of particles with a diameter ≤ this value. D10 and D90 have analogous meaning. Samples with the lowest concentration (0.05 wt%) could not be measured reliably by SLS and thus, the corresponding values are missing. All evaluated statistical parameters (mean size, D10, D50, and D90) of the volume distributions

9

Fig. 6 Volume particle size distribution of original ND⁻ powder measured by SLS
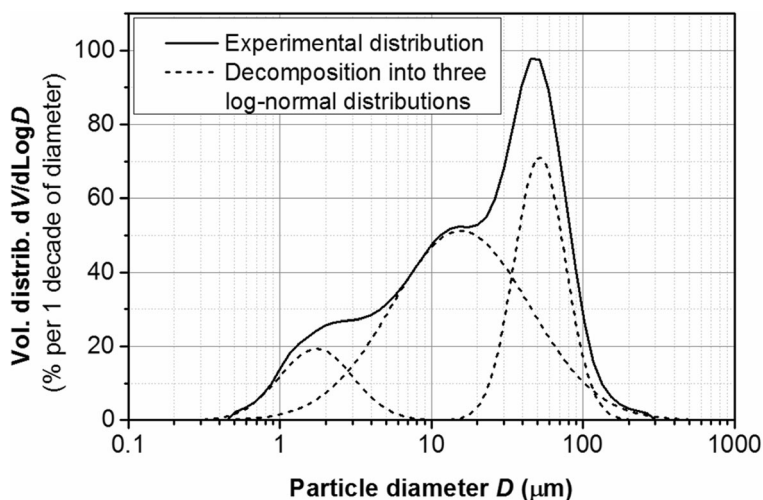
resulting from both SLS and DLS are summarized in Table S3 (Online Resource).

SAXS/USAXS

SAXS and USAXS experiments were performed on both series of samples (in DI water and DMF). Figure 10 shows joined SAXS/USAXS profiles of selected samples of ND⁻ dispersions. The profiles show two knees (Guinier regions) connected with a power-law dependence ($I \propto q^{-d_f}$) showing a non-integer exponent around -2.5. This can be interpreted as due to mass-fractal aggregate structure. Fractal aggregates are random aggregates of particles with a self-similar structure over a certain range of length scales (Mandelbrot 1977). The basic particles building the aggregates are called primary particles. The typical characteristics of a mass-fractal is a decreasing density from the center of the aggregate to its edges. The aggregate mass is proportional to the power of its radius, $m \propto r^{d_f}$. The exponent, d_f ($1 < d_f < 3$) is called fractal dimension and in general it is a

Fig. 7 The visual appearance of ND⁻ dispersions in different weight concentrations for **a** DI water and **b** DMF
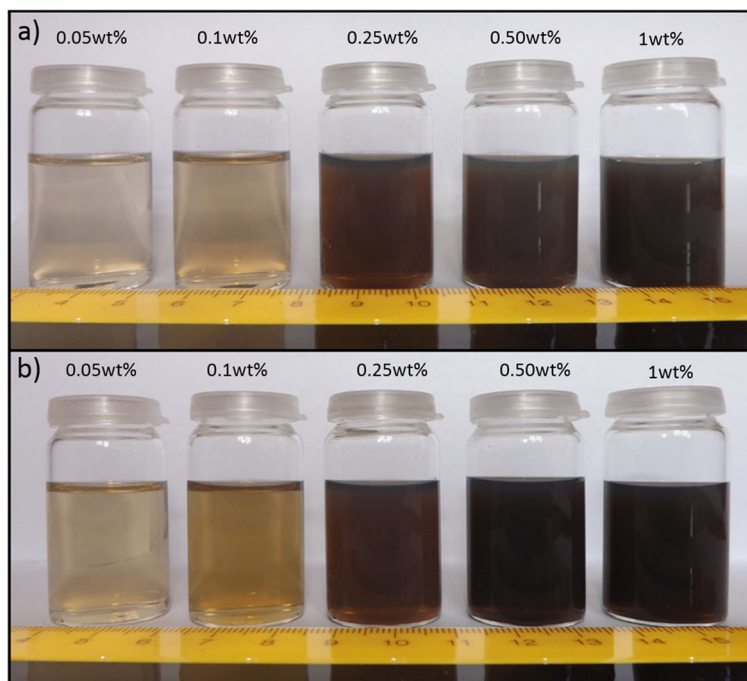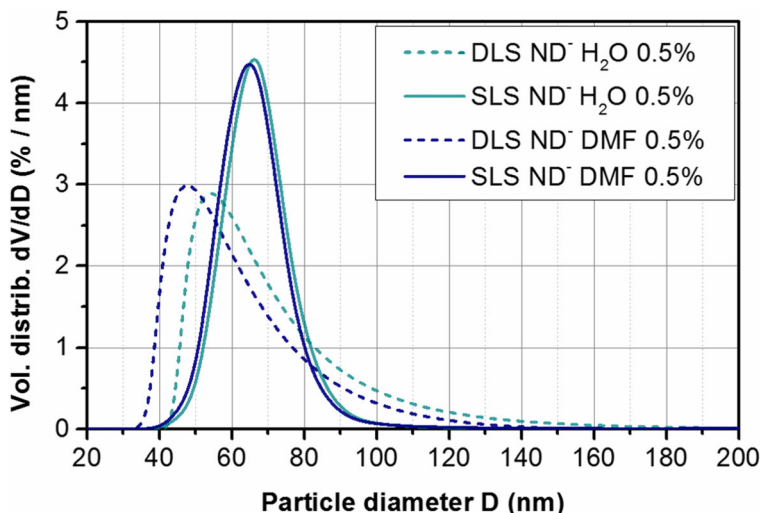
Fig. 8 Volume particle size distribution of ND$^-$ dispersions with concentration 0.5 wt% for DI water and DMF, measured by SLS and DLS techniques

non-integer. Based on the above relationship between the mass and the dimension, a fractal aggregate can be viewed as an object with a non-integer dimension (even though it is a 3D object, of course). The higher the fractal dimension, the denser is the aggregate structure. Such aggregates are formed in various materials, for example silica colloids (silica gel), and the structure of such aggregates can be analyzed by small-angle scattering techniques (Schaefer et al. 1984; Rai et al. 2018). It is well-known that also nanodiamonds in dispersions show the mass-fractal structure (Tomchuk et al. 2015). The fractal dimension d_f corresponds approximately to the magnitude of the exponent of the power-law dependence between the two Guinier regions in the SAXS profile.

To evaluate the size and structural parameters of the aggregates, the profiles were fitted with models using the *Irena* software package (Ilavsky and Jemian 2009) utilizing the unified exponential/power-law approach (Beaucage 1995). Figure 11 shows such a model fit to the joined SAXS/USAXS profile of DMF 0.25% sample. The main parameters provided by the model are R_g (gyration radius) of the primary ND$^-$ particles forming the aggregates, R_g of aggregates, and the fractal dimension of aggregates, d_f. The position of the upper boundary of the power-law region, i.e., the Guinier region at high q around 0.1 A^{-1}, determines the dimension of primary particles—the basic ND$^-$ particles (building blocks of the aggregates). On the other hand, the lower boundary of the power-law dependence, i.e., the knee at low-q values, is due to the aggregates alone and its position is connected with the aggregates size. Thus, by SAXS/USAXS, not only the aggregates size can be studied but also their inner structure. Table 1 summarizes the SAXS/USAXS results for all samples in both series (in DI water and DMF).
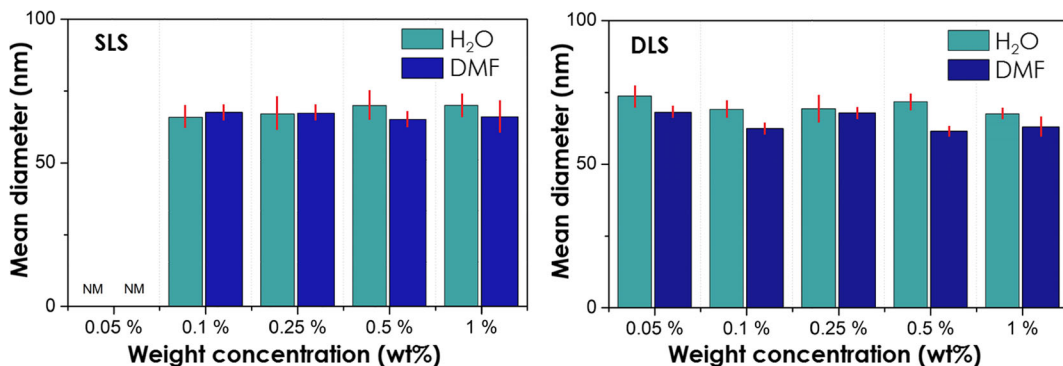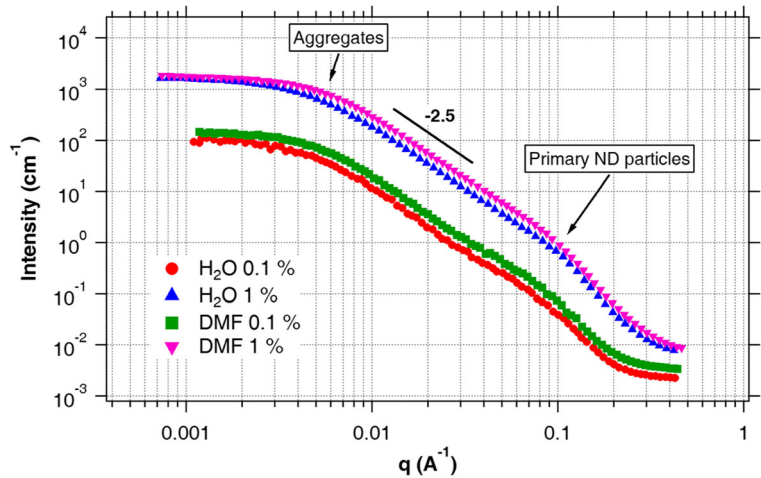

Fig. 9 Mean diameter values of ND$^-$ dispersions by SLS and DLS (NM = non-measurable)

Fig. 10 Joined SAXS/USAXS profiles of selected ND⁻ dispersion samples

Based on the model fitting, the size (namely, the double of their R_g) of the aggregates ranged from 57.0 to 65.2 nm. The differences in size of aggregates are not significant and they do not show any systematic dependence on the concentration. It can be concluded that the aggregates size results based on SAXS/USAXS correspond well to the results of the light scattering methods.

Concerning the inner structure of aggregates, the $2R_g$ of primary particles ranged from 4.0 to 4.4 nm based on the model fitting in *Irena*. Radius of a homogeneous spherical particle is equal to $\sqrt{5/3}$ times R_g. Under the approximative assumption that the basic nanodiamond particles are homogeneous spheres, diameter of nanodiamond particles can thus be determined as 5.4–5.8 nm. This value is higher than 4.0 nm evaluated from XRD and this difference will be explained by SEM and HRTEM in the next section. The fractal dimension of ND⁻ aggregates was in the range from 2.47 to 2.55 based on the model fitting. Its differences between particular samples were small and it did not show any systematic dependence on concentration.

HRTEM/FESEM

HRTEM of dried dispersions was used for characterization of ND⁻ aggregates/particles in combination with selected area electron diffraction (SAED). As a representative sample, the concentration of 0.5 wt% was chosen for both solutions. Figure 12a shows a representative HRTEM micrograph of dried

water dispersion with the corresponding SAED pattern. The image shows the presence of aggregates with tens of nanometer in size that form larger primary aggregates with hundreds of nanometer. The SAED pattern shows broad diffraction circles of randomly oriented nanodiamonds representing the (111), (220), and (311) crystalline planes.

Moreover, HRTEM and SAED demonstrated the presence of chlorargyrite (indicated by an arrow) with (400) plane orientation (according to JCPDS 00-031-1238) in dried DMF dispersion, as seen in Fig. 12b. This observation confirms previous findings of XRD about the presence of AgCl impurities in DMF dispersion after heat treatment, sonication, and centrifugation, respectively. Figure 12c shows dried water dispersion of ND⁻ under higher magnification. HRTEM shows preferably oriented crystalline structure with the nanoparticles exhibiting interlayer spacing d = 0.212 nm (111) and 0.127 nm (220). This observation is close to the XRD results and corresponds with the cubic diamond structure according to JCPDS 00-006-0675. The nanograin size was also determined in the range of 4.2 to 4.5 nm, which is confirmed by XRD analysis. In addition, Fig. 12c illustrates that crystalline phase is surrounded by two ordered graphene layers (indicated by an arrow) with a total thickness of ~ 0.65 nm (Shames et al. 2002; Petit et al. 2012).

Due to low contrast between the carbon-coated grid and diamond particles, it was not possible to detect any individual ND⁻ particles. However, high-resolution SEM in combination with atomically flat silicon wafer substrate was able to identify even the presence of individual ND⁻
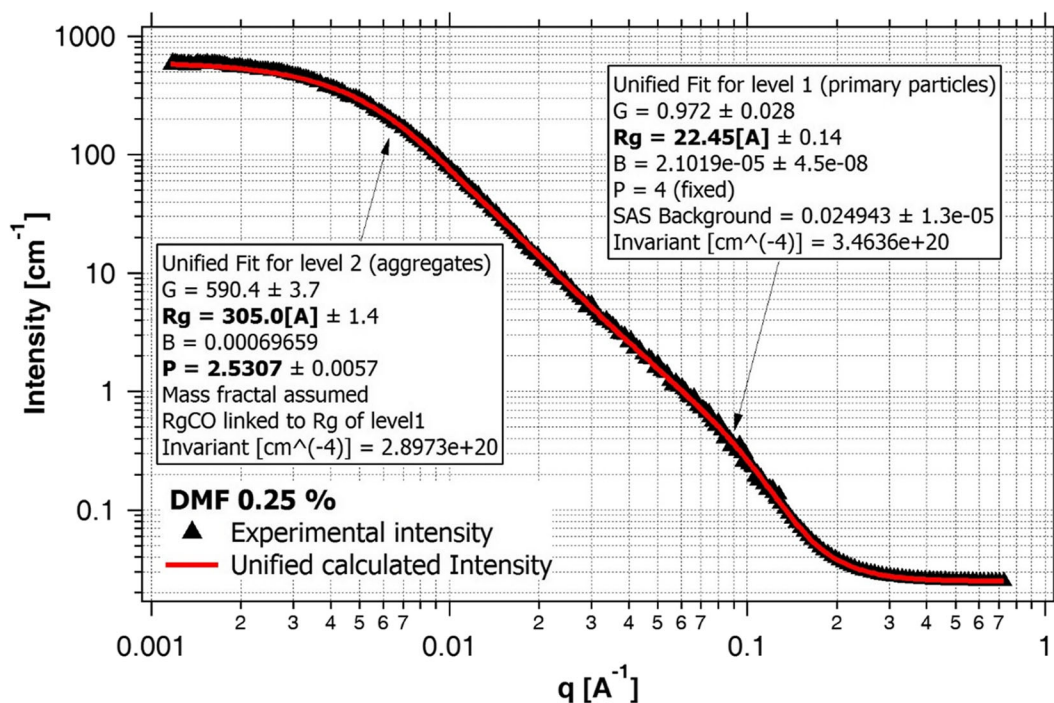
Fig. 11 Joined SAXS/USAXS profile of DMF 0.25% sample together with the unified exponential/power-law model fitted in *Irena*

particles, as shown in Fig. 12d. It was possible mainly due to the better contrast produced by the higher density difference between silicon and diamond, and the flatness of the substrate surface. Based on the findings of HRTEM, we can also explain the difference between the size of primary particles provided by SAXS (5.4–5.8 nm) and XRD (4.0 nm). XRD only evaluates the size of nanodiamond crystallites while SAXS determines the size of the whole particles including the graphene layers.

Conclusion

The presented study deals with the preparation and characterization of ND dispersions in deionized water and DMF. Negatively charged ND dispersions were prepared by oxidative annealing, centrifugation, and sonication. The primary goal of the work was to study the influence of dispersing medium and ND concentration on its aggregation behavior by

Table 1 Summary of results of model fitting to SAXS/USAXS profiles

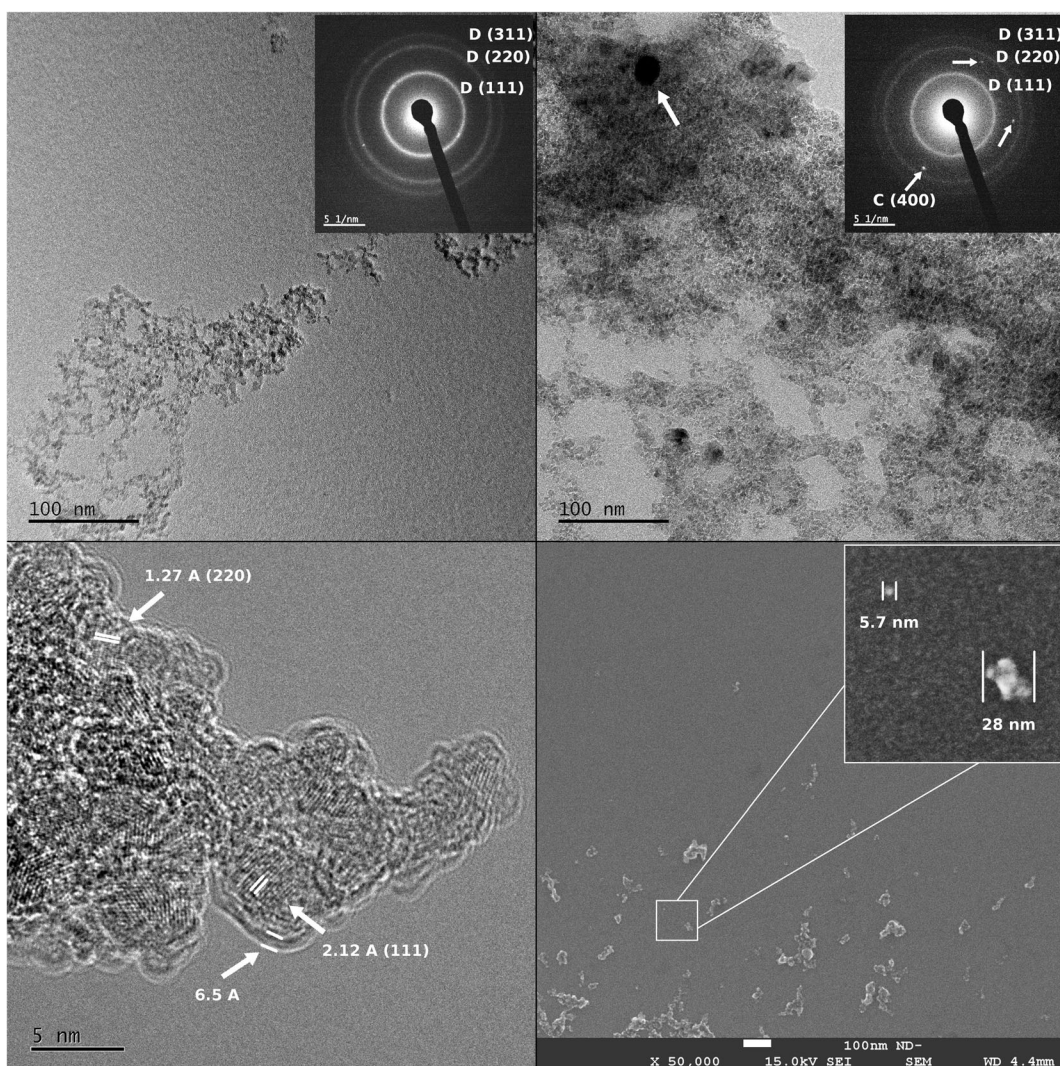| Dispersing medium	Concentration of ND^- (wt%)	$2 \times R_g$ (nm) primary particles	$2 \times R_g$ (nm) aggregates	d_f (−)
DI H_2O	0.05	4.50	60.5	2.47
	0.10	4.40	63.1	2.51
	0.25	4.31	63.1	2.54
	0.50	−	−	−
	1.00	4.20	65.2	2.47
DMF	0.05	4.54	62.7	2.47
	0.10	4.50	61.0	2.51
	0.25	4.49	61.0	2.53
	0.50	4.48	57.2	2.55
	1.00	4.35	57.0	2.54

Fig. 12 HRTEM micrographs of ND⁻ aggregates in **a** dried 0.5 wt% DI water dispersion with the corresponding SAED pattern, **b** dried 0.5 wt% DMF dispersion with SAED pattern, where arrows mark a chlorargyrite crystallite and its corresponding diffraction spots in SAED pattern, and **c** dried water dispersion in high magnification showing crystalline planes of ND cores. **d** FESEM image of dried water dispersion, the high-magnification image in the inset shows an individual ND⁻ particle and an aggregate

various scattering methods. The results showed that both the choice of the dispersing medium (water/DMF) and the ND concentration in the investigated range (0.05–1 wt%) had no significant or systematic influence on the size and inner structure of ND aggregates and thus on the kinetics of the ND aggregate formation. Similar aggregate size was indicated by all the scattering methods used (SLS, DLS, SAXS/USAXS). SLS and DLS gave a mean size between 61 and 73 nm and SAXS/USAXS provided an aggregate size ($2R_g$) in the range from 57 to

65 nm. HRTEM and FESEM also showed the presence of ND aggregates with tens of nanometers in size, in qualitative agreement with the scattering methods.

Besides, the size and structural parameters of primary ND particles were evaluated with various diffraction and scattering methods. The structural data provided by the methods used (XRD, SAXS, HRTEM, SAED, FESEM) are in very good agreement with the JCPDS database and also among each other, as summarized in Table S4 (Online Resource).

14

References

Akinfiev NN, Zotov AV (2016) Solubility of chlorargyrite (AgCl(cr./l.)) in water: new experimental data and a predictive model valid for a wide range of temperatures (273–873K) and water densities (0.01–1g·cm−3). Geochim Cosmochim Acta 178:178–194. https://doi.org/10.1016/j.gca.2016.01.027

Aqel A, Abou El-Nour KMM, Ammar RAA, Al-Warthan A (2012) Carbon nanotubes, science and technology part (I) structure, synthesis and characterization. Arab J Chem 5:1–23. https://doi.org/10.1016/j.arabjc.2010.08.022

Beaucage G (1995) Approximations leading to a unified exponential/power-law approach to small-angle scattering. J Appl Crystallogr 28:717–728. https://doi.org/10.1107/S0021889895005292

Chantooni MK, Kolthoff IM (1973) Solubility product and anionic complexation constants of silver halides, benzoate, and acetate in acetonitrile, N,N-dimethylformamide, and dimethyl sulfoxide. J Phys Chem 77(1):1–7. https://doi.org/10.1021/j100620a001

Dolmatov VY, Lapchuk NM, Lapchuk TM, Nguyen BTT, Myllymäki V, Vehanen A, Yakovlev RY (2016) A study of defects and impurities in doped detonation nanodiamonds by EPR, Raman scattering, and XRD methods. J Superhard Mater 38(4):219–229. https://doi.org/10.3103/S1063457616040018

Huang H, Dai L, Wang DH, Tan L-S, Osawa E (2008) Large-scale self-assembly of dispersed nanodiamonds. J Mater Chem 18:1347–1352. https://doi.org/10.1039/B716676A

Ilavsky J, Jemian PR (2009) Irena: tool suite for modeling and analysis of small-angle scattering. J Appl Crystallogr 42:347–353. https://doi.org/10.1107/S0021889809002222

Ilavsky J, Zhang F, Andrews RN, Kuzmenko I, Jemian PR, Levine LE, Allen AJ (2018) Development of combined microstructure and structure characterization facility for in situ and operando studies at the advanced photon source. J Appl Crystallogr 51(3):867–882. https://doi.org/10.1107/S160057671800643X

Ioni YV, Tkachev SV, Bulychev NA, Gubin SP (2011) Preparation of finely dispersed nanographite. Inorg Mater 47(6):597–602. https://doi.org/10.1134/S0020168511060100

Kaur R, Badea I (2013) Nanodiamonds as novel nanomaterials for biomedical applications: drug delivery and imaging systems.

Int J Nanomedicine 8:203–220. https://doi.org/10.2147/IJN.S37348

Khan M, Shahzad N, Xiong C, Zhao TK, Li T, Siddique F, Ali N, Shahzad M, Ullah H, Rakha SA (2016) Dispersion behavior and the influences of ball milling technique on functionalization of detonated nano-diamonds. Diam Relat Mater 61:32–40. https://doi.org/10.1016/j.diamond.2015.11.007

Kloprogge JT, Ruan HD, Frost RL (2002) Thermal decomposition of bauxite minerals: infrared emission spectroscopy of gibbsite, boehmite and diaspore. J Mater Sci 37:1121–1129. https://doi.org/10.1023/A:1014303119055

Kondo T, Neitzel I, Mochalin VN, Urai J, Yuasa M, Gogotsi Y (2013) Electrical conductivity of thermally hydrogenated nanodiamond powders. J Appl Physiol 113:214307. https://doi.org/10.1063/1.4809549

Koniakhin SV, Besedina N, Kirilenko DA, Shvidchenko A (2017) Ultracentrifugation for ultrafine nanodiamond fractionation. Superlattice Microst 113:201–212. https://doi.org/10.1016/j.spmi.2017.10.039

Krueger A (2008) The structure and reactivity of nanoscale diamond. J Mater Chem 18:1485–1492. https://doi.org/10.1039/B716673G

Krueger A, Kataoka F, Ozawa M, Fujino T, Suzuki Y, Aleksenskij AE, Vul AY, Ōsawa E (2005) Unusually tight aggregation in detonation nanodiamond: identification and disintegration. Carbon 43(8):1722–1730. https://doi.org/10.1016/j.carbon.2005.02.020

Krueger A, Liang Y, Jarre G, Stegk J (2006) Surface functionalisation of detonation diamond suitable for biological applications. J Mater Chem 16:2322–2328. https://doi.org/10.1039/B601325B

Lamouri S (2017) Control of the γ-alumina to α-alumina phase transformation for an optimized alumina densification. Boletín de La Sociedad Española de Cerámica y Vidrio 56:47–54. https://doi.org/10.1016/j.bsecv.2016.10.001

Li C-C, Huang C-L (2010) Preparation of clear colloidal solutions of detonation nanodiamond in organic solvents. Colloid Surface A 353:52–56. https://doi.org/10.1016/j.colsurfa.2009.10.019

Liang Y, Meinhardt T, Jarre G, Ozawa M, Vrdoljak P, Schöll A, Reinert F, Krueger A (2011) Deagglomeration and surface modification of thermally annealed nanoscale diamond. J Colloid Interface Sci 354:23–30. https://doi.org/10.1016/j.jcis.2010.10.044

Liu Y, Gu Z, Margrave JL, Khabashesku VN (2004) Functionalization of nanoscale diamond powder: fluoro-, alkyl-, amino-, and amino acid-nanodiamond derivatives. Chem Mater 16(20):3924–3930. https://doi.org/10.1021/cm048875q

Ma T (2014) Oxidant generation on photolysis of silver chloride suspensions: implications to organic contaminant degradation. Ph.D thesis. University of New South Wales. http://handle.unsw.edu.au/1959.4/54088. Accessed August 2019

Maas M (2016) Carbon nanomaterials as antibacterial colloids. Materials 9(8):617. https://doi.org/10.3390/ma9080617

Mandelbrot BB (1977) Fractals: form, chance, and dimension. CA: WH Freeman and Company, San Francisco

Migdisov AA, Williams-Jones AE, Suleimenov OM (1999) Solubility of chlorargyrite (AgCl) in water vapor at elevated

temperatures and pressures. Geochim Cosmochim Acta 63(22):3817–3827. https://doi.org/10.1016/S0016-7037(99)00213-6

Mitev DP, Townsend AT, Paull B, Nesterenko PN (2014) Screening of elemental impurities in commercial detonation nanodiamond using sector field inductively coupled plasma-mass spectrometry. J Mater Sci 49:3573–3591. https://doi.org/10.1007/s10853-014-8036-3

Mochalin VN, Shenderova O, Ho D, Gogotsi Y (2012) The properties and applications of nanodiamonds. Nat Nanotechnol 7(1):11–23. https://doi.org/10.1038/nnano.2011.209

Oliver A, Williams OA, Hees J, Dieker C, Jager W, Kirste L, Nebel CE (2010) Size-dependent reactivity of diamond nano-particles. ACS Nano 4(8):824–4830. https://doi.org/10.1021/nn100748k

Osawa E (2008) Monodisperse single nanodiamond particulates. Pure Appl Chem 80(7):1365–1379. https://doi.org/10.1351/pac200880071365

Osswald S, Havel M, Mochalin V, Yushin G, Gogotsi Y (2008) Increase of nanodiamond crystal size by selective oxidation. Diam Relat Mater 17(7–10):1122–1126. https://doi.org/10.1016/j.diamond.2008.01.102

Osswald S, Yushin G, Mochalin V, Kucheyev SO, Gogotsi Y (2006) Control of sp2/sp3 carbon ratio and surface chemistry of nanodiamond powders by selective oxidation in air. J Am Chem Soc 128(35):11635–11642. https://doi.org/10.1021/ja063303n

Ozawa M, Inaguma M, Takahashi M, Kataoka F, Krüger A, Osawa E (2007) Preparation and behavior of brownish, clear nanodiamond colloids. Adv Mater 19:1201–1206. https://doi.org/10.1002/adma.200601452

Paci JT, Man HB, Saha B, Ho D, Schatz GC (2013) Understanding the surfaces of nanodiamonds. J Phys Chem C 117(33):17256–17267. https://doi.org/10.1021/jp404311a

Pedroso-Santana S, Sarabia-Saínz A, Fleitas-Salazar N, Santacruz-Gómez K, Acosta-Elías M, Pedroza-Montero M, Riera R (2017) Deagglomeration and characterization of detonation nanodiamonds for biomedical applications. J Appl Biomed 15(1):15–21. https://doi.org/10.1016/j.jab.2016.09.003

Petit T, Arnault J-C, Girard HA, Sennour M, Kang T-Y, Cheng C-L, Bergonzo P (2012) Oxygen hole doping of nanodiamond. Nanoscale 4:6792–6799. https://doi.org/10.1039/C2NR31655B

Phiri J, Gane P, Maloney TC (2017) General overview of graphene: production, properties and application in polymer composites. Mater Sci Eng B 215:9–28. https://doi.org/10.1016/j.mseb.2016.10.004

Pichot V, Risse B, Schnell F, Mory J, Spitzer D (2013) Understanding ultrafine nanodiamond formation using nano-structured explosives. Sci Rep 3:2159. https://doi.org/10.1038/srep02159

Rai DK, Beaucage G, Vogt K, Ilavsky J, Kammler HK (2018) In situ study of aggregate topology during growth of pyrolytic silica. J Aerosol Sci 118:34–44. https://doi.org/10.1016/j.jaerosci.2018.01.006

Ray MA, Tyler T, Hook B, Martin A, Cunningham G, Shenderova JL (2007) Cool plasma functionalization of nano-crys-talline diamond films. Diam Relat Mater 16:2087–2089. https://doi.org/10.1021/ja042389m

Schaefer DW, Martin JE, Wiltzius P, Cannell DS (1984) Fractal geometry of colloidal aggregates. Phys Rev Lett 52(26):2371–2374. https://doi.org/10.1103/PhysRevLett.52.2371

Shakun A, Vuorinen J, Hoikkanen M, Poikelispää M, Das A (2014) Hard nanodiamonds in soft rubbers: past, present and future—a review. Compos Part A Appl Sci Manuf 64:49–69. https://doi.org/10.1016/j.compositesa.2014.04.014

Shames AI, Panich AM, Kempiński W, Alexenskii AE, Baidakova MV, Dideikin AT, Osipov VY, Siklitski VI, Osawa E, Ozawa M, Vul AY (2002) Defects and impurities in nanodiamonds: EPR, NMR and TEM study. J Phys Chem Solids 63(11):1993–2001. https://doi.org/10.1016/S0022-3697(02)00185-3

Shenderova O, Panich AM, Moseenkov S, Hens SC, Kuznetsov V, Vieth HM (2011) Hydroxylated detonation nanodiamond: FTIR, XPS, and NMR studies. J Phys Chem C 115(39):19005–19011. https://doi.org/10.1021/jp205389m

Shenderova OA, Zhirnov VV, Brenner DW (2002) Carbon nano-structures. Crit Rev Solid State Mater Sci 27:227–356. https://doi.org/10.1080/10408430208500497

Singh B, Smith SJ, Jensen DS, Jones HF, Dadson AE, Farnsworth PB, Vanfleet R, Farrer JK, Linford MR (2016) Multi-instrument characterization of five nanodiamond samples: a thorough example of nanomaterial characterization. Anal Bioanal Chem 408(4):1107–1124. https://doi.org/10.1007/s00216-015-9207-z

Song J, Roh J, Lee I, Jang J (2013) Low temperature aqueous phase synthesis of silver/silver chloride plasmonic nanopar-ticles as visible light photocatalysts. Dalton Trans 42(38):13897–13904. https://doi.org/10.1039/C3DT51343B

Sotowa K-I, Amamoto T, Sobana A, Kusakabe K, Imato T (2004) Effect of treatment temperature on the amination of chlori-nated diamond. Diam Relat Mater 13(1):145–150. https://doi.org/10.1016/j.diamond.2003.10.029

Stehlik S, Glatzel T, Pichot V, Pawlak R, Meyer E, Spitzer D, Rezek B (2015) Water interaction with hydrogenated and oxidized detonation nanodiamonds—microscopic and spec-troscopic analyses. Diam Relat Mater 63:97–102. https://doi.org/10.1016/j.diamond.2015.08.016

Stehlik S, Varga M, Ledinsky M, Miliaieva D, Kozak H, Skakalova V, Mangler C, Pennycook TJ, Meyer JC, Kromka A, Rezek B (2016) High-yield fabrication and prop-erties of 1.4 nm nanodiamonds with narrow size distribution. Sci Rep 6:38419. https://doi.org/10.1038/srep38419

Stevenson K, McVey AF, Clark IBN, Swain PS, Pilizota T (2016) General calibration of microbial growth in microplate readers. Sci Rep 6:38828. https://doi.org/10.1038/srep38828

Ten KA, Pruuel ER, Titov VM (2012) SAXS measurement and dynamics of condensed carbon growth at detonation of con-densed high explosives. J Fuller Nanotub Car N 20:587–593. https://doi.org/10.1080/1536383X.2012.656542

Tomchuk OV, Volkov DS, Bulavin LA, Rogachev AV, Proskurnin MA, Korobov MV, Avdeev MV (2015) Structural character-istics of aqueous dispersions of detonation nanodiamond and their aggregate fractions as revealed by small-angle neutron scattering. J Phys Chem C 119(1):794–802. https://doi.org/10.1021/jp510151b

Turner S, Lebedev OI, Shenderova O, Vlasov II, Verbeeck J, Tendeloo GV (2009) Determination of size, morphology, and nitrogen impurity location in treated detonation nanodiamond by transmission electron microscopy. Adv

Funct Mater 19(13):2116–2124. https://doi.org/10.1002/adfm.200801872

Volkov DS, Proskurnin MA, Korobov MV (2014) Elemental analysis of nanodiamonds by inductively-coupled plasma atomic emission spectroscopy. Carbon 74:1–13. https://doi.org/10.1016/j.carbon.2014.02.072

Vul A, Shenderova O (2014) Detonation nanodiamonds: science and applications. Pan Stanford Publishing, Singapore

Xu XY, Zhu Y, Wang B, Yu Z, Xie S (2005) Mechanochemical dispersion of NDs aggregates in aqueous media. J Mater Sci Technol 21:109–112

Zeiger M, Jackel N, Mochalin VN, Volker P (2016) Review: carbon onions for electrochemical energy storage. J Mater Chem A 4:3172–3196. https://doi.org/10.1039/C5TA08295A